Precipitation formation from orographic cloud seeding

Jeffrey R. French[a,1], Katja Friedrich[b], Sarah A. Tessendorf[c], Robert M. Rauber[d], Bart Geerts[a], Roy M. Rasmussen[c], Lulin Xue[c], Melvin L. Kunkel[e], and Derek R. Blestrud[e]

[a]Department of Atmospheric Science, University of Wyoming, Laramie, WY 82071; [b]Department of Atmospheric and Oceanic Sciences, University of Colorado Boulder, Boulder, CO 80309; [c]Research Applications Laboratory, National Center for Atmospheric Research, Boulder, CO 80307; [d]Department of Atmospheric Sciences, University of Illinois Urbana–Champaign, Urbana, IL 61801; and [e]Department of Resource Planning and Operations, Idaho Power Company, Boise, ID 83702

Edited by Dennis L. Hartmann, University of Washington, Seattle, WA, and approved December 19, 2017 (received for review October 1, 2017)

Throughout the western United States and other semiarid mountainous regions across the globe, water supplies are fed primarily through the melting of snowpack. Growing populations place higher demands on water, while warmer winters and earlier springs reduce its supply. Water managers are tantalized by the prospect of cloud seeding as a way to increase winter snowfall, thereby shifting the balance between water supply and demand. Little direct scientific evidence exists that confirms even the basic physical hypothesis upon which cloud seeding relies. The intent of glaciogenic seeding of orographic clouds is to introduce aerosol into a cloud to alter the natural development of cloud particles and enhance wintertime precipitation in a targeted region. The hypothesized chain of events begins with the introduction of silver iodide aerosol into cloud regions containing supercooled liquid water, leading to the nucleation of ice crystals, followed by ice particle growth to sizes sufficiently large such that snow falls to the ground. Despite numerous experiments spanning several decades, no direct observations of this process exist. Here, measurements from radars and aircraft-mounted cloud physics probes are presented that together show the initiation, growth, and fallout to the mountain surface of ice crystals resulting from glaciogenic seeding. These data, by themselves, do not address the question of cloud seeding efficacy, but rather form a critical set of observations necessary for such investigations. These observations are unambiguous and provide details of the physical chain of events following the introduction of glaciogenic cloud seeding aerosol into supercooled liquid orographic clouds.

clouds | precipitation | cloud seeding | radar observations | airborne observations

Following discoveries that silver iodide (AgI) can act as an effective ice nucleant (1) and that introducing dry ice into a supercooled cloud can also produce ice crystals (2), several research projects spanning many decades were conducted to evaluate the efficacy of cloud seeding to enhance precipitation. Glaciogenic seeding relies on the hypothesis that, under appropriate meteorological conditions, the addition of a seeding agent into a cloud of supercooled liquid droplets will cause some of the water droplets to be converted to ice crystals. These crystals subsequently grow through vapor deposition, riming, and aggregation to sizes large enough to eventually fall to the surface as precipitation (3). After decades of experiments that failed to produce definitive results (4), the basic premise of how glaciogenic cloud seeding works was called into question (5). The United States federal government mostly abandoned funding for cloud seeding research in the late 1980s due to the lack of "convincing scientific proof of the efficacy of intentional weather modification" as noted in a 2003 report from the US National Research Council (6). Despite this, the National Research Council committee recommended a coordinated and sustained research effort in cloud and precipitation microphysics, cloud dynamics and modeling, and cloud seeding. Recommendations included "capitalizing on new remote and in situ observational tools" to conduct exploratory and confirmatory experiments.

Despite the absence of scientific proof for the efficacy of glaciogenic seeding of orographic clouds, operational cloud seeding has continued in most states in the western United States and in other countries (7), driven by increased demands for water supplies, the need for hydroelectric power, and the reduction of mountain snowpack. A renewed interest in investigations to examine orographic cloud seeding as a means to produce additional water has arisen (8–11). These recent studies used a statistical approach to determine whether seeding impacted orographic precipitation, along with airborne measurements and radars to examine the clouds for seeding impact. However, these studies have not provided any strong physical or statistical evidence confirming (or refuting) the basic hypothesis upon which glaciogenic seeding relies.

Direct observations of ice crystal formation and evolution through the fallout of precipitation due to glaciogenic seeding are rare. Studies that examine in detail the physical chain of events that results from glaciogenic seeding require multiple observations within a seeded cloud region as the ice particles evolve, descend, and are carried downwind toward the mountain range. Airborne in situ measurements have demonstrated ice crystal formation and subsequent growth through riming and deposition following seeding of supercooled orographic clouds with AgI (12, 13), but were not able to document precipitation formation and fallout of the crystals to the surface. No unambiguous radar measurements demonstrating the chain of events due to glaciogenic seeding with AgI have ever been reported. Radar measurements following airborne seeding with dry ice in a supercooled stratus cloud were obtained using a vertically pointing K_a-band radar (14), but these provided no information about the spatiotemporal evolution of the seeded

Significance

Nearly two decades ago, the National Academy of Sciences commissioned the National Research Council (NRC) to report on *Critical Issues in Weather Modification Research*. The 2003 NRC report highlighted the need to address key uncertainties in our understanding of cloud seeding. Operational cloud seeding continues in nearly a dozen western states, despite a lack of any strong physical evidence supporting its effectiveness. Here, the full chain of events from ice initiation through crystal growth and fallout of snow has been documented. These observations are critical to our understanding of how cloud seeding works and will help direct future research efforts into the effectiveness of cloud seeding.

Author contributions: J.R.F., K.F., S.A.T., R. M. Rauber, B.G., R. M. Rasmussen, L.X., M.L.K., and D.R.B. designed research; J.R.F., K.F., S.A.T., R. M. Rauber, B.G., R. M. Rasmussen, L.X., M.L.K., and D.R.B. performed research; J.R.F., K.F., S.A.T., R. M. Rauber, B.G., and R. M. Rasmussen analyzed data; and J.R.F., K.F., S.A.T., R. M. Rauber, B.G., and R. M. Rasmussen wrote the paper.

The authors declare no conflict of interest.

This article is a PNAS Direct Submission.

Data deposition: All flight-level datasets are available for WKA flight level data, particle probes on the WKA, the WCR, and the DOW radars, at the SNOWIE data archive website (data.eol.ucar.edu/master_list/?project=SNOWIE).

[1]To whom correspondence should be addressed. Email: jfrench@uwyo.edu.

This article contains supporting information online at www.pnas.org/lookup/suppl/doi:10.1073/pnas.1716995115/-/DCSupplemental.

region. An airborne W-band radar was used to document a localized increase in radar reflectivity downwind of ground-based AgI generators in a single case of a shallow mixed-phase orographic cloud (15), but this increase could not be unambiguously attributed to seeding, in part due to the lack of in situ observations. These studies have presented evidence that suggest that treating wintertime orographic clouds containing supercooled liquid with glaciogenic seeding material might impact precipitation characteristics, such as the size and concentration of ice crystals. However, the full physical evolution of the treated cloud through ice initiation to precipitation growth and fallout has yet to be documented.

Evaluating the efficacy of cloud seeding is a multistep process. The first step is to establish the physical chain of events that occurs when seeding material is introduced into a supercooled cloud. Once this is established, the next step is to determine the conditions under which these changes (due to seeding) occur and how often they might exist for a particular region. Following that, one needs to determine how much additional snow falls to the surface under seeded conditions and integrate over several storm systems or an entire season. The objective of this manuscript is to document the first step in this process: demonstrating the causal sequence of events that occurs following the glaciogenic seeding of a supercooled cloud with AgI.

Herein, we present radar and in situ observations from two cases that provide the strongest evidence, to date, of the full microphysical chain of events following airborne glaciogenic seeding of orographic cloud systems. In this study, we were able to observe, with high spatial and temporal resolution, the processes of glaciogenic seeding from the release of the AgI, the conversion of supercooled liquid into ice particles, their subsequent growth into precipitation, and fallout to the surface. The data were collected during the 2017 Seeded and Natural Orographic Wintertime Clouds: The Idaho Experiment (SNOWIE), conducted from January through March over the Payette Mountains of southwestern Idaho.

Cloud Seeding Experiments

The experiments described herein utilized two ground-based radars, a cloud physics research aircraft, and a seeding aircraft, to release, track, and measure the impact of glaciogenic seeding material released into orographic cloud systems. In SNOWIE, AgI aerosols were released from a specially modified B200 King Air, hereafter referred to as the "seeding aircraft." The seeding aircraft used pyrotechnic flares to release the AgI. These aerosols are submicron and hence follow air trajectories, dispersing downstream in the smoke plume from the burning flares. Flares were either burn-in-place (BIP), resulting in a continuous line of AgI along the flight track, or ejectable (EJ), dropped from the aircraft at discrete intervals, resulting in a quasi-vertical line of AgI extending roughly 820 m below the level of the aircraft (Fig. 1). BIPs were most often used when the seeding aircraft was flying through or at the level of the targeted cloud; EJs were used when the seeding aircraft was above the top of the targeted cloud. Repeated, wind-perpendicular tracks were flown upwind of the target region, releasing AgI that was subsequently carried downwind through the cloud.

Fig. 1 shows the hypothesized behavior of pockets of ice crystals following AgI interactions with supercooled water and their resulting radar reflectivity, hereafter referred to as seeding signatures. As the AgI nuclei intersperse with supercooled liquid water at temperatures colder than about −7 °C, some droplets are expected to freeze (16). The newly formed ice crystals are then expected to grow first through vapor deposition and then more rapidly through riming of cloud droplets and aggregation with other ice particles. These much larger hydrometeors should be detectable by cloud and precipitation radar, since radar reflectivity is highly sensitive to particle size. Ideal conditions for

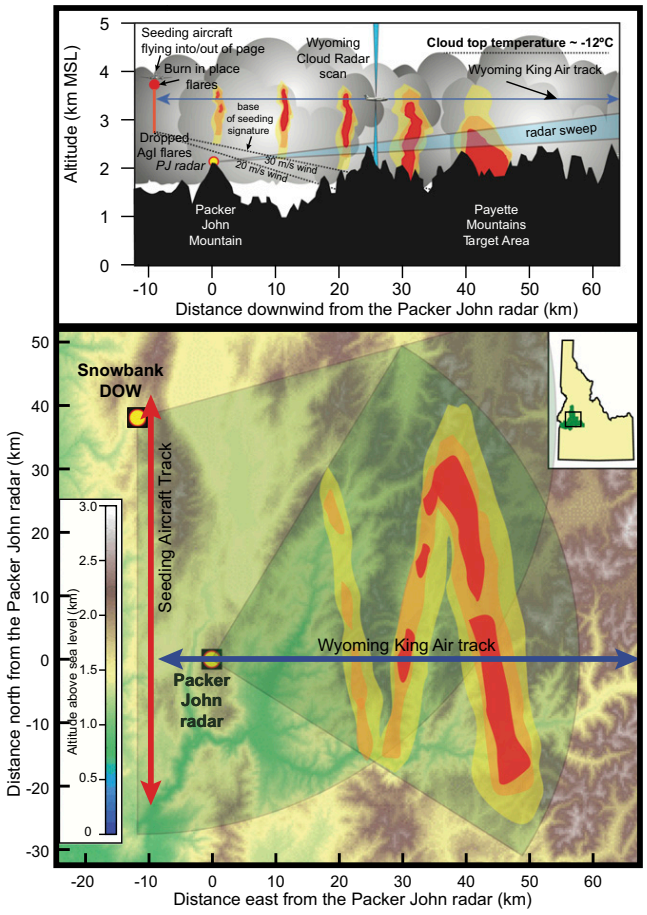

Fig. 1. A conceptual illustration of the anticipated seeding signature and the experimental setup as part of SNOWIE. In both panels, the yellow–orange–red colors indicate locations and relative magnitude of radar returns. Yellow dots show locations of ground-based radars, red lines represent typical flight tracks for the seeding aircraft, and blue lines are flight tracks for WKA. (*Bottom*) A plan view and (*Top*) a vertical cross-section along the flight track of the WKA. Seeding material is released either as BIP or EJ flares (see *Cloud Seeding Experiments*). Vertical depth of echoes as a function of downwind distance depends, in part, on wind speed. The bases of the radar echo descend as particles grow and fall, illustrated by the dashed line in the *Top* for two different wind speeds. Here, we assume constant wind speed with height. Wind direction is from west to east (left to right across the figure).

detecting seeding signatures from radar rely on natural clouds devoid of ice. Such clouds contain supercooled liquid droplets no larger than a few hundred microns in diameter and produce radar reflectivity (Z) of no more than about −5 dB relative to Z (dBZ). Once ice is initiated, the crystals can grow to millimeter size in several hundred seconds and result in reflectivity of 10 to 20 dBZ (or greater), producing a clear signal compared with the background natural cloud.

In the horizontal view (Fig. 1, *Bottom*), the seeding signatures that result from the growing ice crystals downwind of the AgI release are expected to appear in a widening zig-zag pattern, since the seeding material is released at discrete times and locations along the seeding aircraft's track. The widening of the seeding signatures with increasing distance downwind is expected, due to turbulence, solenoidal response to latent heat release by freezing (17), and differential fall velocities of particles. In the vertical view (Fig. 1, *Top*), the altitude at which ice crystals form due to interactions of supercooled water droplets with AgI nuclei is expected to roughly coincide with the flight level of the seeding

aircraft (if flown through cloud as shown in the figure) or the top of the cloud and below (if the aircraft releases EJ flares no more than ~820 m above cloud top). The bases of the seeding signatures are expected to descend downwind as ice crystals grow and fall out of the base of the cloud. The distance downwind at which the seeding signatures intersect the mountain surface depends on the rate of growth and terminal fall speed of the ice particles, the magnitude of the wind, vertical wind shear, and turbulence. The use of EJ flares, which results in an extension of AgI aerosol well below the flight level of the seeding aircraft, should produce a distinctly different pattern of ice than that produced through seeding with BIP flares or even by the aircraft themselves. This is an important distinction, since aircraft can initiate ice in a supercooled liquid cloud through a combination of mechanisms (17–19). EJ flares also allow for seeding to occur when the seeding aircraft is flown well above cloud top.

Two X-band "Doppler on Wheels" (DOW) scanning radars (20), located at mountaintop locations at Packer John and Snowbank (Fig. 1), surveyed the area using both horizontal (Plan Position Indicator; PPI) and vertical (Range Height Indicator; RHI) scan strategies. In these winter clouds, meteorological radar signals above the background noise result from scattering by precipitating ice particles. An instrumented aircraft operated by the University of Wyoming (Wyoming King Air, WKA; refs. 21 and 22) flew wind-parallel legs typically below the flight level of the seeding aircraft and directly over the Packer John radar site. The WKA was instrumented with a vertically pointing (up and down) W-band radar (Wyoming Cloud Radar, WCR; ref. 22) capable of retrieving fine-scale cross-sections of radar reflectivity along the flight track. Because of its short wavelength, the WCR detects scattered radiation from both cloud droplets and larger ice crystals. The combined use of W-band and X-band radars allows observation of the development and evolution of both cloud and precipitation particles. The WKA also carried several particle spectrometers and other instruments for directly measuring basic thermodynamic parameters, total condensed and liquid water content, and cloud hydrometeor size, shape, and concentration along its flight path. Descriptions of the instruments used in this study, the measurements they provide, and processing and limitations of the dataset are provided in *Supporting Information*.

The WKA flew repeated tracks along a geographically fixed path roughly aligned with the wind. The first and second legs were conducted before the arrival of the seeding aircraft to document natural conditions. Following this, the seeding aircraft released AgI for 1 h to 2 h along tracks perpendicular to the wind. During this time, and after the seeding aircraft vacated the area, the WKA continued sampling the region as the plume moved downwind over the mountains. Because of the orientation of the flight tracks, any ice crystals produced by the WKA passing through clouds (17–19) would result in enhanced reflectivity aligned with the wind, rather than across the wind, and be readily distinguishable from echoes resulting from release of AgI from the seeding aircraft.

Seeding Case #1. Fig. 2 shows radar reflectivity from the Packer John DOW radar over a 60-min period during case #1. Seeding began at 0000 Coordinated Universal Time (UTC) and continued for eight legs, concluding at 0130 UTC. EJ flares were released on all legs about every 30 s, corresponding to 3-km spacing along the flight track. BIPs were used only on flight legs 2 to 5 and leg 8. Before 0030 UTC, the DOW detected only a few small radar reflectivity echoes in excess of 10 dBZ, 30 km to 40 km east of Packer John. Between 0030 UTC and 0100 UTC, radar echoes with reflectivity between 15 dBZ and 25 dBZ began to appear 5 km to 35 km SE of Packer John. The first two lines farthest downwind at 0100 UTC clearly show individual isolated areas of enhanced reflectivity spaced at about 3 km, identical to

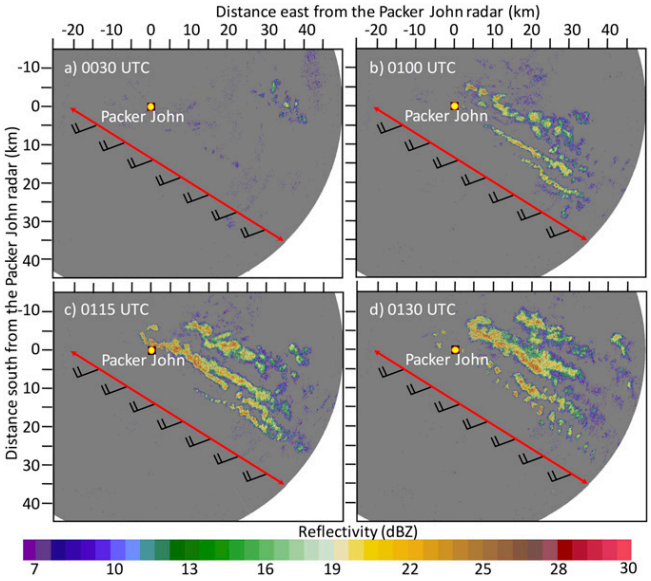

Fig. 2. PPI of radar reflectivity from the ground-based DOW radar located at Packer John mountaintop for case #1 at four time periods over 60 min: (*A*) 0030, (*B*) 0100, (*C*) 0115, and (*D*) 0130 UTC. The scans were conducted at 2° elevation angle and, therefore, show the reflectivity just above ground level close to the radar to roughly 1.7 km above ground level at 50-km range. The red line indicates the track of the seeding aircraft, which was repeated eight times (see *Seeding Case #1*). Wind barbs plotted on the aircraft track illustrate mean wind direction and speed (in meters per second) at flight level. Each barb is 10 $m \cdot s^{-1}$.

spacing of EJ releases and distinctly different from a pattern that would be produced due to AgI released through BIPs or ice produced by the aircraft themselves, both of which should result in a continuous line. As these lines of enhanced reflectivity moved downwind, they broadened and merged. Subsequent lines of enhanced reflectivity with maximum values between 20 dBZ and 30 dBZ appeared between 0100 UTC and 0115 UTC, continuous due to the use of both BIP and EJ flares. Variations along lines were likely due to spatial heterogeneity in wind and cloud properties. A zig-zag pattern of continuous radar reflectivity lines was readily visible at 0115 UTC. Lines of isolated reflectivity maxima that began to appear at 0130 UTC resulted from the use of EJ flares only in seeding legs 6 and 7. The reflectivity lines continued to be visible until 0255 UTC, after which the area largely became devoid of radar echoes again.

Seeding Case #2. Measurements from case #2 revealed enhanced radar reflectivity from two seeding lines from both EJ and BIP flares and provided a comprehensive set of observations from ground-based radar and from airborne in situ and radar measurements through the entire evolution of the seeding plume. In this case, the seeding aircraft flew a total of six legs. The first two legs were flown at 4 km above mean sea level (MSL), just at the top of cloud at that time. However, on all subsequent legs, the seeding aircraft flew at 4.5 km above MSL, about 1 km above cloud top. EJ flares released at this altitude burned out before entering the cloud, and thus these legs were too high to impact precipitation formation with AgI seeding material. A line of enhanced reflectivity with maximum value of about 20 dBZ first appeared roughly 45 min after completion of the first seeding leg (Fig. 3, 1710 UTC). The line appeared about 30 km downwind of the track of the seeding aircraft, and extended from near Packer John on its northwestern end to the southeast edge of the radar scan. At this same time, the vertical dimension of the line (Fig. 4) extended from cloud top, about 4 km above MSL, to just above

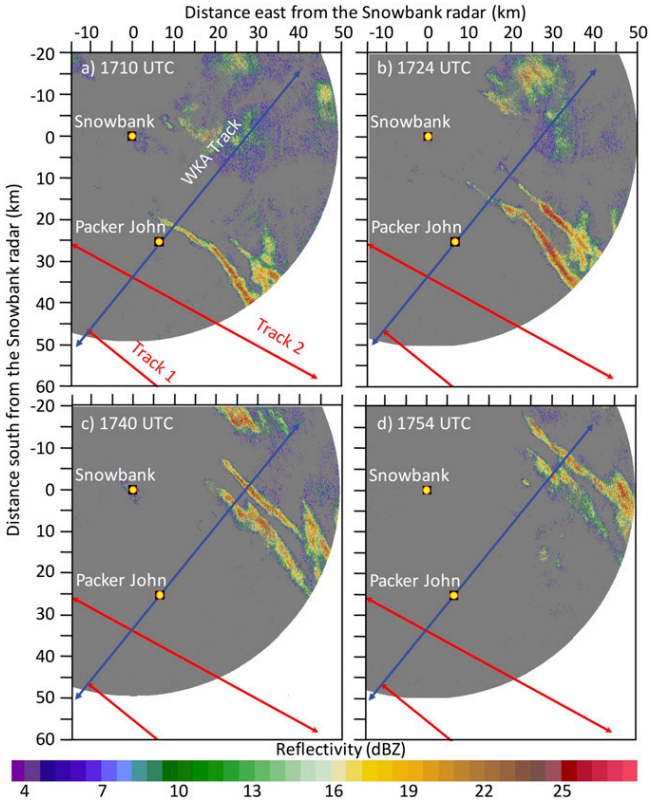

Fig. 3. PPI of radar reflectivity at 2° elevation angle from the ground-based DOW radar located at Snowbank mountaintop for case #2 at four time periods over ∼45 min: (*A*) 1710, (*B*) 1724, (*C*) 1740, and (*D*) 1754 UTC. Red lines indicate the two seeding tracks completed (track 1: 1619 UTC to 1629 UTC; track 2: 1641 UTC to 1650 UTC), with arrows to indicate the direction of each track. Subsequent tracks were flown at higher altitudes and are not shown. The blue line indicates the flight track of the WKA (Fig. 5) and the azimuth of the RHI scans from DOW radar at Packer John shown in Fig. 4.

the surface. The reflectivity return had a strong tilt due to a differential wind speed of about 5 m·s^{-1} between 3 km and 4 km above MSL. Fifteen minutes later, at 1724 UTC, a second line was readily visible about 5 km downwind of the first. The appearance of this line, on the downwind side of the first line, resulted from the seeding aircraft shifting roughly 17 km downwind for its second flight leg. Subsequent scans from both DOW radars allowed the horizontal and vertical evolution of these two lines to be tracked. By 1740 UTC, both lines extended from cloud top to the surface, and their maximum reflectivity increased from 20 dBZ to >28 dBZ. As the reflectivity lines reached the northeastern portion of the study area, the radar signals in the lower portions became blocked by terrain.

Over a 75-min period, the WKA passed through or just below the seeding lines seven times. At 1629 UTC, the seeding aircraft passed 28 km directly upwind of Packer John radar on its first flight leg. Assuming a steady wind speed of 11 m·s^{-1} based on WKA measurements, by 1651 UTC, the seeding material and any newly formed ice crystals would have advected 14.5 km downwind, to a location ∼13.5 km upwind of the radar. On its first leg at 1651 UTC, the WKA passed below an area of enhanced reflectivity, detected by the WCR, about 12.5 km upwind of the Packer John radar site (Fig. 5), within 1 km of the expected location of the seeded region. The WKA was at an altitude of 3.6 km MSL, 500 m to 1,000 m below cloud top, at a temperature of −11.5 °C. The region of enhanced reflectivity extended from flight level to the top of the cloud and had maximum reflectivity of 5 dBZ, about 20 dBZ to 30 dBZ greater than reflectivity at that altitude in the surrounding area. In situ probes on the WKA indicated that the cloud at this level outside the seeded regions was composed mostly of liquid water droplets, with mean diameter of about 20 μm, concentration of 25 cm^{-3}, and a liquid water content of about 0.08 g·m^{-3} (Fig. 6). At flight level, ice water content was below the detection limit of the probe, less than 0.01 g·m^{-3}.

Seven minutes later, at 1658 UTC, the region of enhanced reflectivity had descended through the WKA flight level and increased to 10 dBZ (Fig. 5). The maximum reflectivity was located 500 m above flight level and the same distance below cloud top. The enhanced reflectivity line was 7 km upwind of Packer John; the expected location of the seeding line assuming simple advection and a constant wind speed was 8.5 km upwind. In the line, at flight level, the liquid water was 0.04 g·m^{-3}, reduced by half from the first pass. The ice water content, however, increased to 0.15 g·m^{-3}. Measurements from cloud particle spectrometers indicate that the ice particles ranged in diameter from a few hundred microns to about 1 mm, in concentrations of about 4 L^{-1}, compared with concentrations outside of the line of 10^{-2} L^{-1}. Particle images suggest that the crystals were moderately rimed. In the region a few kilometers downwind of the enhanced reflectivity, the cloud remained devoid of ice, and liquid water content ranged between 0.05 g·m^{-3} and 0.10 g·m^{-3}.

During the time between the first and second pass, the region of enhanced reflectivity drifted about 5.5 km, consistent with WKA flight-level wind measurements. The location of the reflectivity region during each of these passes relative to the location (and time) that the seeding material was released match to within 1 km to 2 km, assuming a constant 11 m·s^{-1} wind speed. Recall also that, at 1710 UTC, the first seeding line was detected by ground-based radar at an altitude between 3 km and 4 km above MSL about 3 km downwind of Packer John (Fig. 4). The enhanced reflectivity detected by the WCR during the WKA's second pass at 1658 UTC drifted ∼10 km by 1710 UTC and was located just downwind of Packer John, confirming that this enhanced reflectivity echo was the seeding line detected by the ground-based radars.

At 1718 UTC, the WKA made a third pass through the first (upwind) seeding line. By this time, the radar signature from the WCR extended from cloud top down to the surface. The second

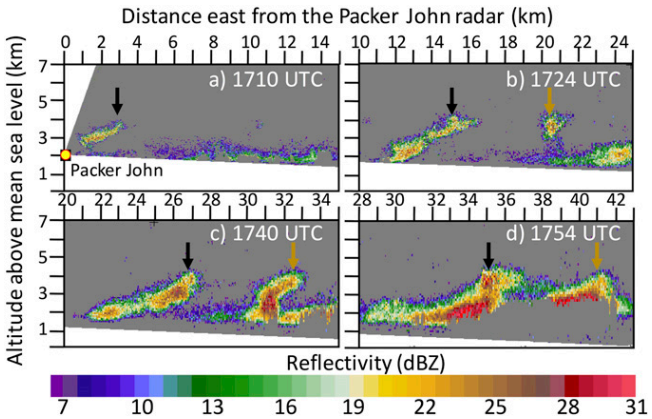

Fig. 4. Vertical cross-section of radar reflectivity downwind of the Packer John radar site for case #2 at the same time periods shown in Fig. 3: (*A*) 1710, (*B*) 1724, (*C*) 1740, and (*D*) 1754 UTC. The scans were conducted along the flight track of the WKA (blue line in Fig. 3). The black arrow indicates the top of the enhanced echo due to the first seeding plume; the gold arrow shows the location due to the second seeding plume. Note that the horizontal scale changes for each of the four panels as the echoes drift with the mean horizontal wind. In *C* and *D*, some portions of the lowest part of the echoes are blocked due to the surface and the higher terrain in those locations.

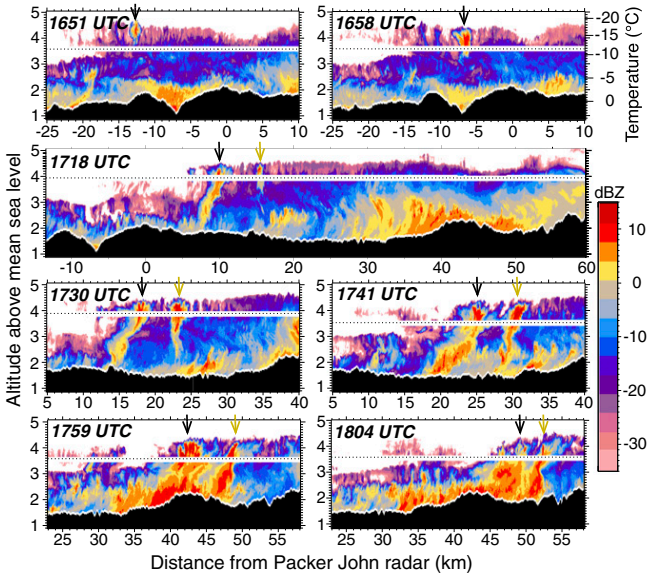

Fig. 5. Vertical cross-section of radar reflectivity from the WCR for seven passes in case #2. The times at which the aircraft passed through the first seeding signature (location indicated by the black arrows) are labeled in each panel. Radar reflectivity for the entire leg length is shown for the third leg at 1718 UTC; for all others, a 35-km length roughly centered on the seeding line(s) is shown. The black arrows denote the center of the first seeding signature, and gold arrows denote the location of the second. The black dotted line in each panel indicates the flight level of the WKA; the white area directly above and below this is the ~200-m "dead zone" not detected by the radar. The black regions near the bottom in each panel show the underlying terrain. A temperature scale, taken from a sounding launched at 1625 UTC, is shown on the right side of *Top Right*,.

seeding line was also detectable from the WCR reflectivity return, near the top of the cloud, 5.5 km downwind of the first line. For this pass and the subsequent one at 1730 UTC, the WKA ascended to 3.9 km above MSL, about 500 m below cloud top where the temperature was −13.5 °C. In the first seeding line, none of the in situ probes detected any supercooled liquid. Maximum ice water contents were 0.15 g·m^{-3}, and in situ probes detected ice in a 2-km-wide area. Ice particles were mixed between moderately rimed and branched crystals, suggestive of growth through vapor deposition. Particle size distributions (Fig. 6, *Bottom Right*) indicate that the mean (maximum) diameter for the ice crystal population was about 1 mm (4 mm) within the seeding line at flight level. Concentrations of particles with diameters less than about 70 μm were small, at or below the detection level of the probes. For larger particles, concentrations were 0.8 L^{-1}. Conversely, outside of the seeding line, all of the particles detected were smaller than 100 μm and appeared to be liquid. In the second seeding line, which was first detected by the WCR at 1718 UTC, much of the water mass had not yet been converted to ice at flight level. Maximum cloud liquid water contents were 0.06 g·m^{-3}, as were ice water contents.

By the time the WKA passed through the seeding lines again, at 1730 UTC, the lines had widened to 2.5 km to 3.0 km at flight level, and maximum ice water content had increased to 0.25 g·m^{-3} in the first line and 0.35 g·m^{-3} in the second. Little liquid water remained in either line, less than 0.05 g·m^{-3} at flight level. In the first line, most particles had grown to diameters in excess of 1 mm, and crystals as large as 8 mm in diameter were detected. Nearly all of the crystals appeared to be branched dendrites with only a light degree of riming. In the second line, crystals were smaller, with a mean diameter about 700 μm, and the crystals were heavily rimed. In both lines, reflectivity from the WCR had increased to a maximum of about 10 dBZ within about 500 m of the flight level of the WKA, and ice crystal concentrations for particles larger than 300 μm in diameter were 1 L^{-1} to 5 L^{-1}. Concentrations outside of the seeded regions were less than 0.1 L^{-1}.

Between 1741 UTC and 1804 UTC, the WKA made three more passes as the seeding lines continued to drift downwind over the mountains. During these passes, the WKA flew at 3.6 km above MSL. By 1741 UTC, WCR reflectivity from both seeding lines extended from cloud top to the ground. No liquid was detected in either of the seeding lines, and maximum ice water contents had decreased to about 0.25 g·m^{-3}. Particle size distributions indicate nearly all ice crystals were between 200 μm and 2 mm in diameter, with a mean size of about 500 μm, significantly smaller than earlier passes. During the last two passes at 1759 UTC and 1804 UTC, the >10-dBZ reflectivity region extended over nearly the entire vertical extent of the echo, with very little liquid water (<0.05 g·m^{-3}) at flight level. Ice water content in excess of 0.45 g·m^{-3} was observed at flight level in the first seeding line at 1759 UTC, but it decreased to just over 0.10 g·m^{-3} in the subsequent pass. Below the level of the WKA, the WCR radar return from just above the surface suggests a region of hydrometeor growth with higher reflectivity extending over a broad area.

Conclusions

In this study, measurements from ground-based X-band radars, an airborne W-band cloud radar, and in situ cloud physics probes were presented that together provide the strongest evidence yet for the initiation and growth of ice crystals as the result of glaciogenic seeding with AgI, leading to precipitation (snow) on a mountain surface within a specific target region. These observations, in two separate cases, showed the initial appearance of cloud seeding signatures within 30 min following the release of AgI in the cloud. Seeding lines were tracked, and the evolution of ice crystals to precipitating snow was documented. At the

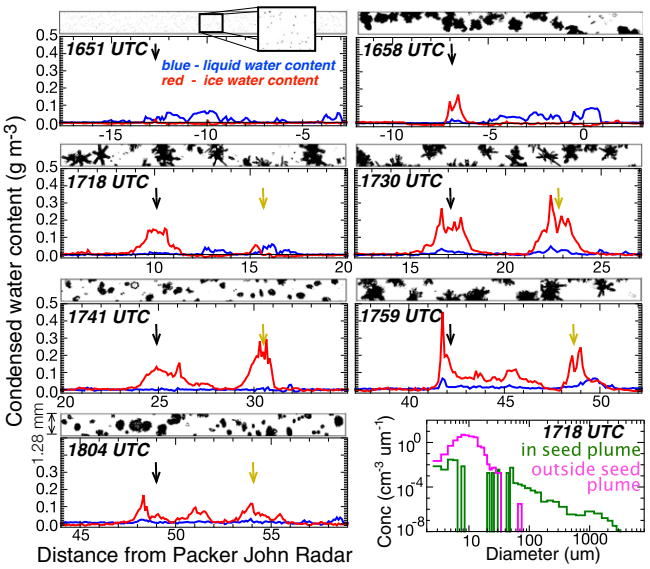

Fig. 6. Condensed water mass (ice in red, liquid in blue) measured by in situ probes on the WKA for a 15-km length in each of the seven passes shown in Fig. 5. Arrows indicate center of seeding plumes (as in Fig. 5). The box above each time trace contains sample images of particles from within the first seeding plume during that pass. For scale, the height of the box corresponds to 1.28 mm. The very tiny images from the pass at 1651 UTC are cloud droplets ($d \approx 20$ μm) with a zoomed section included. *Bottom Right* shows particle size distributions taken from the third pass at 1718 UTC. The green line is from inside the seeding line, and the magenta line is from outside of the seeding line.

flight level of the WKA, concentrations of ice crystals with diameter greater than 300 μm remained at 1 L^{-1} to 5 L^{-1} after the nucleation of ice particles, two to three orders of magnitude greater than values consistently observed outside of the seeding lines in natural cloud conditions at the same altitude. Shortly after the initial detection of ice, crystals at flight level were moderately rimed, and mean particle diameter was a few hundred microns. Later in the evolution, as supercooled liquid was depleted, crystals at flight level continued to grow through vapor deposition and aggregation. Mean particle diameters exceeded 1 mm, and the largest ice crystals grew to 8 mm in diameter. Such large crystals did fall to the surface, as evidenced by the extension of the radar reflectivity downward to the surface with time. However, the seeding signals persisted throughout the depth of the cloud, even near cloud top, for 60 min to 90 min following the completion of seeding, suggesting that ice continued to nucleate well downwind of the initial release.

These comprehensive observations provide unambiguous evidence that glaciogenic seeding of a supercooled liquid cloud can enhance natural precipitation growth in a seeded cloud, leading to precipitation that would otherwise not fall within the targeted region. They further provide information that is critical to advance our understanding of how cloud seeding works and under what conditions seeding will have an impact on the evolution of clouds and precipitation. However, this study does not directly address cloud seeding effectiveness. Rather, observations such as these are a necessary component for investigations into the efficacy of cloud seeding and, as such, can be utilized in future investigations to quantify cloud seeding impact.

Materials and Methods

All data presented here are publicly available through the SNOWIE data archive website maintained by the Earth Observing Laboratory (EOL) at the National Center for Atmospheric Research (NCAR). The URL is provided in *Supporting Information*. Data are archived in NetCDF or ASCII format, and each dataset contains an accompanying text file providing necessary metadata. Description of calibration and uncertainties for DOW, WCR, and in situ cloud instruments on the WKA are also provided in *Supporting Information*.

ACKNOWLEDGMENTS. We greatly appreciate the superb and laborious efforts of the crews from the DOW radars from the Center of Severe Weather Research (CSWR), in particular, Dr. Karen Kosiba, Dr. Joshua Wurman, Traeger Meyer, Marcus Guitierrez, Andrew Frambach, and Paul Robinson; from the WKA at the University of Wyoming, in particular, Dr. Sam Haimov, Dr. Larry Oolman, Dr. David Plummer, Matt Burkhart, Zane Little, Brent Glover, Ben Heesen, Tom Drew, and Brett Wadsworth; and from the cloud seeding aircraft from Weather Modification International (WMI) for their dedication during very difficult and exhausting operating conditions in cold and windy snowstorms. We thank the graduate and undergraduate students from the University of Colorado (Josh Aikins and Robinson Wallace), University of Wyoming (Adam Tripp, Adam Majewski, and Spencer Faber), and University of Illinois (Adam Springer and Andrew Janiszeski) for their help operating and deploying instruments during the campaign. Funding for CSWR-DOWs and WKA was provided through National Science Foundation (NSF) Grants AGS-1361237 and AGS-1441831, respectively. Funding for WMI seeding aircraft was provided by Idaho Power Company. The research was supported under NSF Grants AGS-1547101, AGS-1546963, and AGS-1546939.

1. Vonnegut B (1947) The nucleation of ice formation by silver iodide. *J Appl Phys* 18: 593–595.
2. Schaefer VJ (1946) The production of ice crystals in a cloud of supercooled water droplets. *Science* 104:457–459.
3. Ludlam FH (1955) Artificial snowfall from mountain clouds. *Tellus* 7:277–290.
4. Kerr RA (1982) Cloud seeding: One success in 35 years. *Science* 217:519–521.
5. Rangno AL (1986) How good are our conceptual models of orographic cloud seeding. *Precipitation Enhancement A Scientific Challenge*, Meteorological Monograph (Am Meteor Soc, Boston), Vol 43, pp 115–126.
6. National Research Council (2003) *Critical Issues in Weather Modification Research* (Natl Acad Press, Washington, DC).
7. Qiu J, Cressey D (2008) Meteorology: Taming the sky. *Nature* 453:970–974.
8. Manton MJ, et al. (2011) A confirmatory snowfall enhancement project in the Snowy Mountains of Australia. Part I: Project design and response variables. *J Appl Meteorol Climatol* 50:1432–1447.
9. Breed D, et al. (2014) Evaluating winter orographic cloud seeding: Design of the Wyoming Weather Modification Pilot Project (WWMPP). *J Appl Meteorol Climatol* 53:282–299.
10. Pokharel B, Geerts B (2016) A multi-sensor study of the impact of ground-based glaciogenic seeding on clouds and precipitation over mountains in Wyoming. Part I: Project description. *Atmos Res* 182:269–281.
11. Pokharel B, et al. (2017) A multi-sensor study of the impact of ground-based glaciogenic seeding on clouds and precipitation over mountains in Wyoming. Part II: Seeding impact analysis. *Atmos Res* 183:42–57.
12. Deshler T, Reynolds DW, Huggins AW (1990) Physical response of winter orographic clouds over the Sierra Nevada to airborne seeding using dry ice or silver iodide. *J Appl Meteorol* 29:288–330.
13. Deshler T, Reynolds DW (1990) The persistence of seeding effects in a winter orographic cloud seeded with silver iodide burned in acetone. *J Appl Meteorol* 29:477–488.
14. Hobbs PV, et al. (1981) Radar detection of cloud-seeding effects. *Science* 213: 1250–1252.
15. Chu X, Geerts B, Xue L, Pokharel B (2017) A case study of cloud radar observations and large eddy simulations of a shallow stratiform orographic cloud, and the impact of glaciogenic seeding. *J Appl Meteorol Climatol* 56:1285–1304.
16. Boe BB, DeMott PJ (1999) Comparisons of Lohse wing-tip nuclei generators and burn-in-place pyrotechnics in the North Dakota Cloud Modification Project. *J Weather Mod* 31:109–118.
17. Heymsfield AJ, et al. (2011) Formation and spread of aircraft-induced holes in clouds. *Science* 333:77–81.
18. Rangno A, Hobbs PV (1983) Production of ice particles in clouds due to aircraft penetrations. *J Clim Appl Meteorol* 22:214–232.
19. Rangno A, Hobbs PV (1984) Further observations of the production of ice particles in clouds by aircraft. *J Clim Appl Meteorol* 23:985–987.
20. Wurman J, Straka J, Rasmussen E, Randall M, Zahrai A (1997) Design and deployment of a portable, pencil-beam, pulsed, 3-cm Doppler radar. *J Atmos Ocean Technol* 14:1502–1512.
21. Rodi A (2011) King of the air: The evolution and capabilities of Wyoming's observation aircraft. *Meteorol Technol Int* May 2011:44–47.
22. Wang Z, et al. (2012) Single aircraft integration of remote sensing and in situ sampling for the study of cloud microphysics and dynamics. *Bull Am Meteorol Soc* 93:653–668.
23. Haimov S, Rodi A (2013) Fixed-antenna pointing-angle calibration of airborne Doppler cloud radar. *J Atmos Ocean Technol* 30:2320–2335.
24. University of Wyoming Flight Center (1995) University of Wyoming Cloud Radar (WCR). Available at dx.doi.org/10.15786/M2237S. Accessed September 1, 2017.
25. Korolev AV, Strapp JW, Isaac GA, Nevzorov AN (1998) The Nevzorov airborne hot-wire LWC–TWC probe: Principle of operation and performance characteristics. *J Atmos Ocean Technol* 15:1495–1510.
26. Korolev A, Strapp JW, Isaac GA, Emery E (2013) Improved airborne hot-wire measurements of ice water content in clouds. *J Atmos Ocean Technol* 30:2121–2131.
27. Abel SJ, Cotton RJ, Barrett PA, Vance AK (2014) A comparison of ice water content measurement techniques on the FAAM BAe-146 aircraft. *Atmos Meas Tech* 7: 3007–3022.
28. Schwarzenboeck A, Mioche G, Armetta A, Herber A, Gayet JF (2009) Response of the Nevzorov hot wire probe in clouds dominated by droplet conditions in the drizzle size range. *Atmos Meas Tech* 2:779–788.
29. Lance S, Brock CA, Rogers D, Gordon JA (2010) Water droplet calibration of the cloud droplet probe (CDP) and in-flight performance in liquid, ice and mixed-phase clouds during ARCPAC. *Atmos Meas Tech* 3:1683–1706.
30. Lance S (2012) Coincidence errors in a cloud droplet probe (CDP) and a cloud and aerosol spectrometer (CAS), and the improved performance of a modified CDP. *J Atmos Ocean Technol* 29:1532–1541.
31. Faber S (2017) Error characterization for airborne cloud probes using laboratory calibration and in-situ analysis. MS thesis (Univ Wyoming, Laramie).
32. Lawson RP, et al. (2006) The 2D-S (Stereo) probe: Design and preliminary tests of a new airborne, high-speed, high-resolution particle imaging probe. *J Atmos Ocean Technol* 23:1462–1477.
33. Knollenberg RG (1981) Techniques for probing cloud microstructure. *Clouds, Their Formation, Optical Properties, and Effects*, eds Hobbs PV, Deepak A (Academic, New York), pp 15–91.
34. Jackson RC, et al. (2014) An assessment of the impact of antishattering tips and artifact removal techniques on cloud ice size distributions measured by the 2D cloud probe. *J Atmos Ocean Technol* 31:2567–2590.
35. Finlon JA, et al. (2016) A comparison of X-band polarization parameters with in situ microphysical measurements in the comma head of two winter cyclones. *J Appl Meteorol* 55:2549–2574.
36. Korolev A, Isaac GA (2005) Shattering during sampling by OAPs and HVPS. Part I: Snow particles. *J Atmos Ocean Technol* 22:528–542.
37. Korolev A, Emery E, Creelman K (2013) Modification and tests of particle probe tips to mitigate effects of ice shattering. *J Atmos Ocean Technol* 30:690–708.
38. Field PR, Heymsfield AJ, Bansemer A (2006) Shattering and particle interarrival times measured by optical array probes in ice clouds. *J Atmos Ocean Technol* 23:1357–1371.
39. University of Wyoming – Flight Center (2017) Flight level data from the University of Wyoming King Air during the Seeded and Natural Orographic Wintertime clouds—the Idaho Experiment (SNOWIE) project, version 1.0. Available at dx.doi.org/10.15786/M2MW9F. Accessed September 1, 2017.
40. University of Wyoming – Flight Center (2017) Wyoming cloud radar data from the University of Wyoming King Air during the Seeded and Natural Orographic Wintertime clouds—the Idaho Experiment (SNOWIE) project, version 1.0. Available at dx.doi.org/10.15786/M2CD4J. Accessed September 1, 2017.